MATERIALS SCIENCE

Copackaging photosensitizer and PD-L1 siRNA in a nucleic acid nanogel for synergistic cancer photoimmunotherapy

Yuanyuan Guo[1,2], Qiushuang Zhang[2], Qiwen Zhu[3], Jing Gao[3], Xinyuan Zhu[2], Haijun Yu[3]*, Yuehua Li[1]*, Chuan Zhang[2]*

Packaging multiple drugs into a nanocarrier with rational design to achieve synergistic cancer therapy remains a challenge due to the intrinsically varied pharmacodynamics of therapeutic agents. Especially difficult is combining small-molecule drugs and macromolecular biologics. Here, we successfully graft pheophorbide A (PPA) photosensitizers on DNA backbone at predesigned phosphorothioate modification sites. The synthesized four PPA-grafted DNAs are assembled into a tetrahedron framework, which further associates with a programmed death ligand-1 (PD-L1) small interfering RNA (siRNA) linker through supramolecular self-assembly to form an siRNA and PPA copackaged nanogel. With dual therapeutic agents inside, the nanogel can photodynamically kill tumor cells and induce remarkable immunogenic cell death. Also, it simultaneously silences the PD-L1 expression of the tumor cells, which substantially promotes the antitumor immune response and leads to an enhanced antitumor efficacy in a synergistic fashion.

INTRODUCTION

Immune escape is one of the key reasons for the genesis and development of tumor, which prevents the mutated cells from attacking by the protective immune cells (*1*). To escape the immune surveillance, the solid tumors usually overexpress various inhibitory checkpoint receptors and recruit suppressive cells such as regulatory T cells (T_{regs}) and myeloid-derived suppressor cells to establish an immunosuppressive microenvironment (*2*, *3*). For instance, the programmed death 1/programmed death ligand-1 (PD-1/PD-L1) signaling pathway is one of the dominant mechanisms of immune evasion, through which tumor cells can disable the activated effector T cells and prevent their tumor cell killing effect (*4*). Immune checkpoint blockade (ICB) therapy against the PD-1/PD-L1 pathway can modulate the immunosuppressive microenvironment of tumor and restore the function of cytotoxic T lymphocytes (CTLs), which have shown great success in clinic practices against a large variety of tumors (*5*). However, the responsive rate to PD-1/PD-L1 ICB therapy in clinic is relatively low (~20%) due to insufficient infiltration of the T cells in the tumor tissues (*6*, *7*). Hence, combining ICB approach with other therapeutic modalities that can evoke tumor immunogenicity and increase T cell infiltration has become hotspots in cancer therapy.

As a noninvasive and specific antitumor therapeutic modality, photodynamic therapy (PDT) can cause cancer cell death by generating cytotoxic reactive oxygen species (ROS) from photosensitizer under laser irradiation (*8*–*10*). Many studies have shown that PDT can induce tumor immunogenic cell death (ICD) and recruit dendritic cells (DCs) to present tumor-associated antigens (TAAs), thereafter activate the effector T cells and induce antitumor immunity (*11*). On the other hand, the therapeutic efficacy of PDT is often impeded by the hydrophobic feature of photosensitizer, limited penetration of laser, and hypoxic and immunosuppressive tumor microenvironment (*12*). Therefore, PDT and ICB therapeutic modalities, in principle, can be nicely coupled together to suppress tumor growth in a synergistic fashion. Photosensitizers have been loaded in micelles (*13*), nanoparticles (*14*–*17*), metal-organic frameworks (*18*), etc. and then combined with ICB monoclonal antibodies (mAbs) to achieve an enhanced photoimmunotherapy (*19*). Because of the intrinsic difference between hydrophobic photosensitizer and macromolecular mAbs, it is usually difficult to copackage them into an integrated nanoplatform, thus sequential administrations of these two therapeutic agents have to be applied in previous studies (*14*). Moreover, the use of ICB antibodies often suffers from poor diffusion, low tumor penetration, and immune-related adverse effects (*20*). The antibody therapeutics only block the immune checkpoints on cell membranes, which could be compensated by the constant expression of proteins in cytoplasm (*21*, *22*). To overcome these issues, RNA interference–based PD-1/PD-L1 knockdown provides an alternative approach to enhance the T cell–mediated tumor killing (*23*, *24*). Compared to mAb inhibitors, small interfering RNA (siRNA) can down-regulate the immune checkpoint proteins from the intracellular source (*25*), which augments the PDT-induced antitumor immune response and achieves enhanced synergistic antitumor effect in combinatorial photoimmunotherapy (*13*). However, delivery challenges likewise still exist in this approach. Although various nanocarriers have been used to copackage the photosensitizer and siRNA, the drug loading capacity, siRNA compression efficiency, and biocompatibility of the carrier materials may not fully satisfy the demanding requirements of cancer treatment (*26*, *27*). Therefore, it is highly desirable to develop new vehicles that can efficiently copackage siRNA and photosensitizer for combinatorial photodynamic immunotherapy.

---

[1] Department of Radiology, Shanghai Jiao Tong University Affiliated Sixth People's Hospital, Shanghai Jiao Tong University School of Medicine, 600 Yi Shan Road, Shanghai 200233, China. [2] School of Chemistry and Chemical Engineering, Frontiers Science Center for Transformative Molecules, Shanghai Key Laboratory for Molecular Engineering of Chiral Drugs, Shanghai Jiao Tong University, 800 Dongchuan Road, Shanghai 200240, China. [3] State Key Laboratory of Drug Research and Center of Pharmaceutics, Shanghai Institute of Materia Medica, Chinese Academy of Sciences, Shanghai 201203, China.

*Corresponding author. Email: chuanzhang@sjtu.edu.cn (C.Z.); liyuehua312@163.com (Y.L.); hjyu@simm.ac.cn (H.Y.)

Recently, DNA has emerged as a novel noncationic carrier with good biocompatibility for drug delivery (*28*). In particular, a few DNA nanostructures, such as siRNA vesicles (siRNAsome) (*29*) and spherical nucleic acids (*30*, *31*), have been used for the codelivery of gene and small-molecule drugs. However, the oligonucleotide payloads are usually immobilized at the outer shell of the DNA nanostructures, making them vulnerable to be digested by nucleases. To protect the therapeutic siRNA, we once proposed a self-assembled nucleic acid nanogel platform for efficient siRNA delivery, in which functional siRNAs were designed to be cross-linkers for nanogel assembly and lastly embedded inside the three-dimensional (3D) architecture (*32*, *33*). On the basis of this strategy, here, we design a PD-L1 siRNA cross-linker and a photosensitizer-bearing DNA tetrahedral framework, which can supramolecularly assemble into a nucleic acid nanogel copackaged with pheophorbide A (PPA) and siRNA (siRNA/PPA-NG; Fig. 1) for combinatorial photoimmunotherapy. In brief, we first covalently graft multiple PPAs onto the backbones of four component DNA strands at the phosphorothioate (PS) modification sites to obtain water-soluble PPA-DNA conjugates, which further assemble into a DNA tetrahedral framework. In our design, a sticky end is introduced at each vertex of the PPA-bearing DNA tetrahedron, which is complementary to the overhangs predesigned on siRNA linker. Last, the sticky end association allows the cross-linking of these two structural units, forming the siRNA/PPA-NG. In this nanogel system, hydrophilic DNA assists the PPAs to homogeneously dissolve in aqueous solution. As a result, the photosensitizer-containing nanogel exhibits excellent water solubility inherited from the nucleic acids, which promotes the $^1O_2$ generation and causes remarkable ICD of the tumor cells to activate the host immune response. Meanwhile, siRNA released from the nanogel would down-regulate PD-L1 expression in the tumor cells and synergistically promote the CTL-mediated tumor killing, thus achieves strong suppression of both the primary and distal tumors. Equipped with small molecular drug and functional nucleic acid therapeutics through simple drug conjugation and programmable nucleic acid self-assembly, our nanogel platform paves an efficient avenue to achieve combinatorial antitumor treatment.

RESULTS

Syntheses and characterizations of PPA-DNA conjugates (PPA-DNAs)

To construct a PPA-bearing DNA tetrahedral framework as structural units for nanogel assembly, first four PS-modified DNA strands with sticky end overhangs (DNA-A to DNA-D, 69 nucleotides; see table S1) according to literature (*34*) were used to conjugate with PPA photosensitizer. Because of the hydrophobic feature of PPA, to ensure the good water solubility of final PPA-DNA conjugates (PPA-DNA-A to PPA-DNA-D), six PS modifications were well dispersedly introduced on the backbone of each component DNA strand. Before the conjugation, benzyl bromide–modified PPA (PPA-Bz-Br) was synthesized via a one-step esterification reaction (Fig. 2A) and analyzed by hydrogen and carbon nuclear magnetic resonance spectra (^{1}H-NMR and ^{13}C-NMR; fig. S1), respectively, in which all peaks could be nicely ascribed to the desired product. The mass spectrometry (MS) exhibits mass/charge ratio (*m*/*z*) values of 717.24 and 719.24, which could be attributed to the $[M + H]^+$ ions of PPA-Bz-Br (fig. S2). Thereafter, the obtained PPA-Bz-Br was

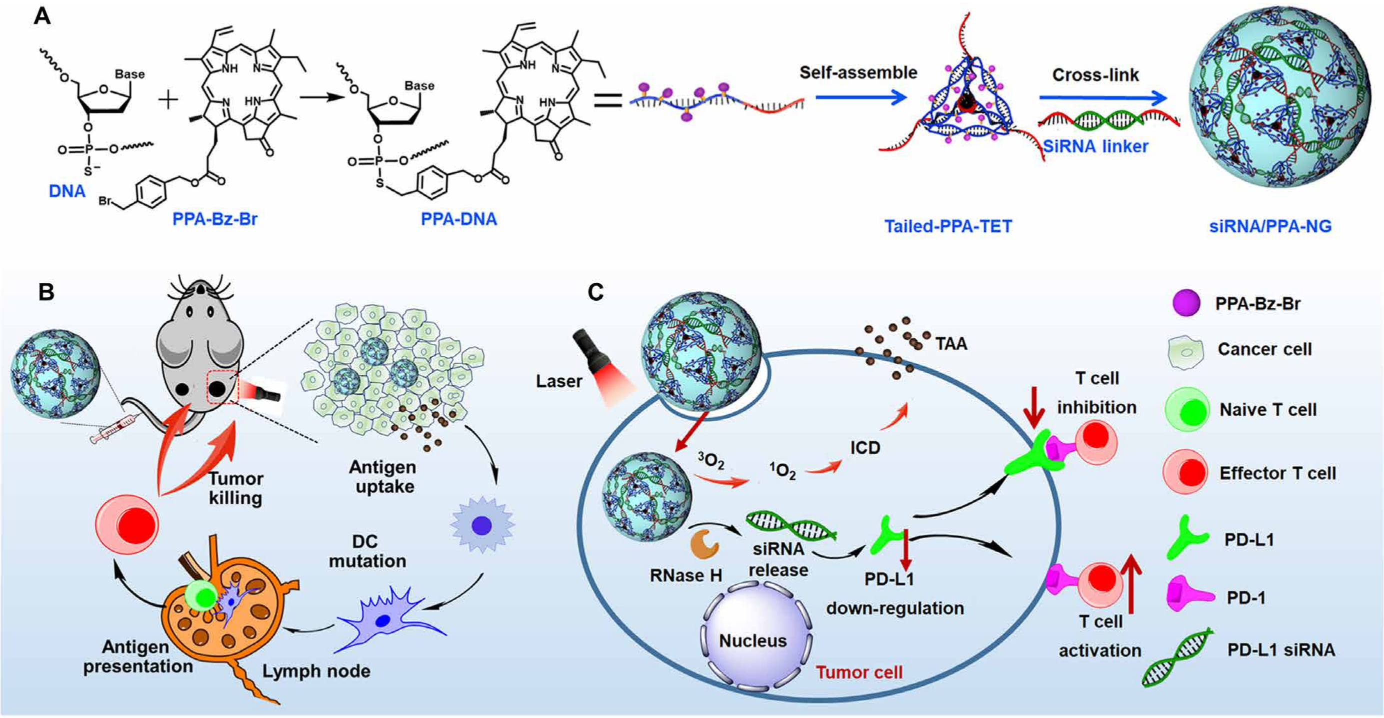

Fig. 1. Schematic illustration of programmed assembly of siRNA/PPA-NG and its synergistic functions in cancer photoimmunotherapy. (**A**) Syntheses of the PPA-DNA conjugates and the self-assemblies of PPA-bearing DNA tetrahedron (tailed-PPA-TET) and siRNA/PPA-NG. (**B**) The process of synergistic cancer photoimmunotherapy mediated by siRNA/PPA-NG in vivo. (**C**) Intracellular synergistic actions of siRNA/PPA-NG in the photoimmunotherapy.

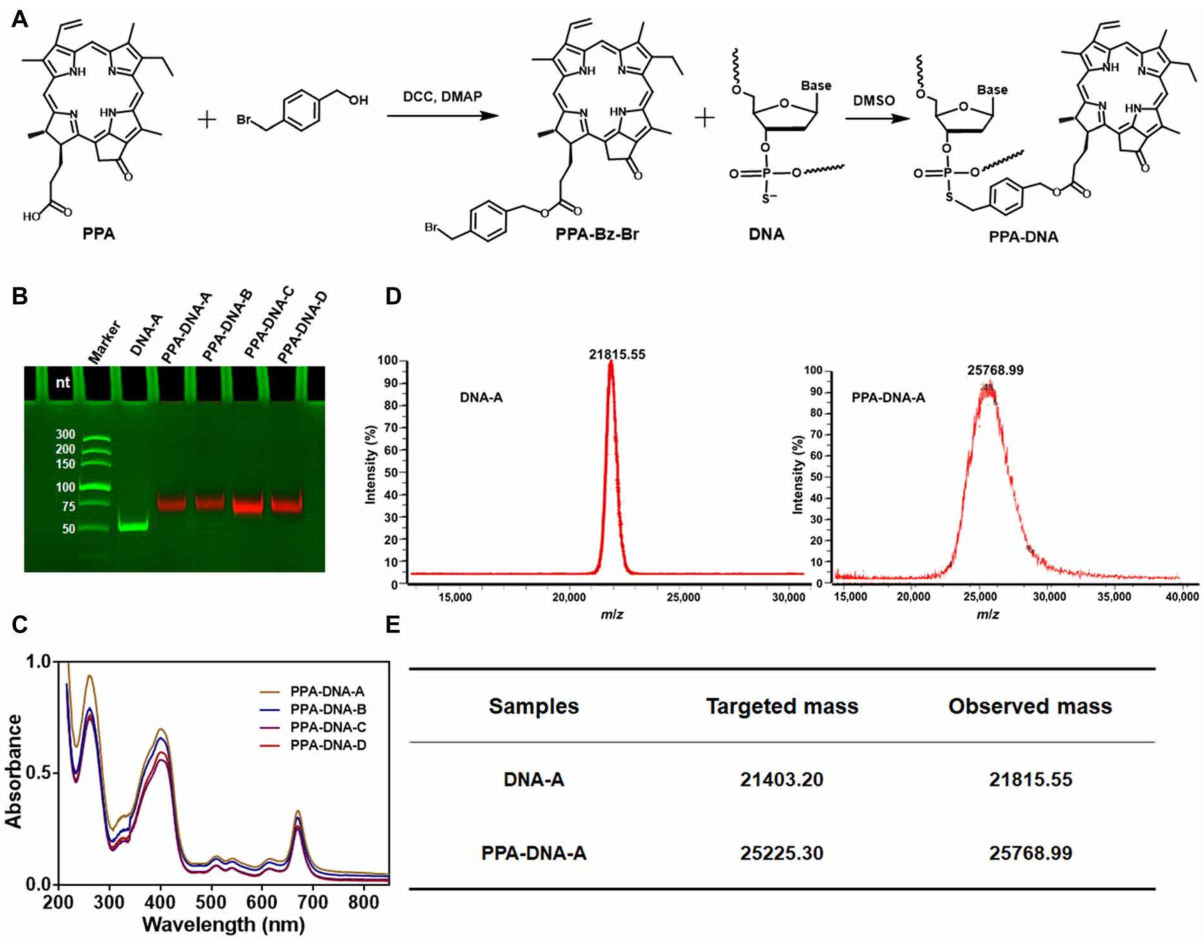

Samples	Targeted mass	Observed mass
DNA-A	21403.20	21815.55
PPA-DNA-A	25225.30	25768.99

Fig. 2. Characterizations of PPA-grafted DNA strands. (**A**) The synthetic route of PPA-DNA conjugates. (**B**) Fifteen percent of denaturing PAGE gel image of the free DNA strand and PPA-DNA conjugates. Four single-stranded DNAs (DNA-A, DNA-B, DNA-C, and DNA-D) were used to graft with PPA, respectively. Green fluorescent bands represent the unmodified DNA strands stained by ethidium bromide (EB). Red fluorescent bands indicate the PPA-grafted DNAs for tetrahedral framework and nanogel self-assembly, which are imaged under a 650-nm channel. nt, nucleotide. (**C**) The UV/vis spectra of the PPA-DNA conjugates. (**D**) Representative MALDI-TOF MS spectra of the unconjugated DNA strand and the corresponding PPA-DNA conjugate. (**E**) Summarized mass of unconjugated DNA and PPA-DNA conjugate based on MS analysis. The number of PPA grafted on DNA is calculated by PPA = $(M_{\text{PPA-DNA}} - M_{\text{DNA}})/(M_{\text{PPA-Bz-Br}} - M_{\text{Br}})$, where $M_{\text{PPA-DNA}}$ is the observed mass of PPA-DNA-A (25768.99), $M_{\text{PPA-DNA}}$ is the observed mass of DNA-A (21815.55), $M_{\text{PPA-Bz-Br}}$ is the molecular mass of PPA-Bz-Br (718), and M_{Br} is the molecular mass of Br (78.9).

reacted with each component PS-DNA at 55°C in dimethyl sulfoxide (DMSO) to synthesize the PPA-DNA conjugates. After purification, the obtained PPA-DNA conjugates were characterized by multiple techniques. First, 15% denaturing polyacrylamide gel electrophoresis (PAGE) was used to demonstrate the purity and hydrophilicity of PPA-DNA conjugates. As shown in Fig. 2B, PPA-DNA conjugates show good solubility and can migrate into the PAGE gel under electrophoresis, as evidenced by the single band in the gel with a slower migration rate than initial unconjugated DNA strand. In addition, ultraviolet/visible (UV/vis) spectra show that PPA-DNA conjugates have characteristic absorbance peaks of both DNA (260 nm) and PPA (the broad peaks at 409 and 667 nm; Fig. 2C), respectively, indicating successful grafting of PPAs onto the DNA strands. Furthermore, molecular weights of free DNA strand and PPA-DNA conjugate were determined by matrix-assisted laser desorption/ionization–time-of-flight MS (MALDI-TOF MS). As an example, the observed *m*/*z* values of PPA-DNA-A conjugate and free DNA-A are 25,768.99 and 21,815.55, respectively (Fig. 2, D and E), indicating that all PS groups on DNA backbone are grafted with PPA molecules, which is consistent with the determination results by UV/vis spectroscopy (fig. S3).

Programmed assembly and characterizations of siRNA/PPA-NG

With PPA-grafted DNA strands, next, we started the preparation of photosensitizer and PD-L1 siRNA copackaged nanogel based on nucleic acid self-assembly. Because drug grafting through PS group does not change the base pairing of modified DNAs, the obtained PPA-DNA conjugates would retain the programmable self-assembly property in the premise of their kept solubility in aqueous solution. The programmed assembly of siRNA/PPA-NG was conducted through two steps: annealing and cross-linking. First, four synthesized PPA-DNA strands were equivalently mixed in tris-acetate-EDTA-Mg^{2+} (TAE/Mg^{2+}) buffer and then quickly annealed from 95° to 4°C, resulting in the formation of PPA-bearing DNA tetrahedron with a sticky end at each vertex (tailed-PPA-TET). Four percent native PAGE and 2% agarose gel electrophoresis were subsequently used to confirm the formation of tailed-PPA-TET. As shown in fig. S4, the self-assembled PPA-bearing DNA tetrahedron exhibits as a single sharp band in the gel and has lower mobility compared to the tetrahedron without drug conjugation (tailed-TET). Afterward, PD-L1 siRNA linkers were mixed with the obtained tailed-PPA-TET in 1× TAE/Mg^{2+} buffer, which further associated together to form siRNA/PPA-NG through DNA/RNA sticky end hybridization (Fig. 1A).

In our experiments, effect of tailed-PPA-TET/linker ratios on nanogel assembly was investigated by 4% native PAGE and 0.5% agarose gel electrophoresis (fig. S5). When tailed-PPA-TET/linker ratio varied from 1:0.5 to 1:2.5, larger aggregates stuck in loading wells could be observed in 4% native PAGE gel (fig. S5A), indicating the successful cross-linking between two building blocks. Note that, with more linker addition, the tailed-PPA-TET band was gradually disappeared, and excessive linker band appeared when the tailed-PPA-TET/linker ratio was beyond 1:2 (fig. S5A). In 0.5% agarose gel, nanogel bands could be obtained with tailed-PPA-TET/linker ratios from 1:1 to 1:1.6, while larger aggregates appeared when tailed-PPA-TET/linker ratio reached 1:1.8 as evidenced by the stuck aggregates in the loading wells (fig. S5B). Thus, 1:1.6 molar ratio of tailed-PPA-TET/siRNA linker was selected for nanogel assembly, which allows the extra tailed-PPA-TET to locate at outside of the nanogel and protect the embedded siRNA linkers. In this condition, hydrodynamic diameter of the as-prepared siRNA/PPA-NG is ~99 nm with a polydispersity index of ~0.2, as determined by dynamic light scattering (DLS; Fig. 3B). In addition, the assembled nanogel shows a spherical morphology as revealed by atomic force microscopy (AFM) imaging (Fig. 3C).

The photoactivity and fluorescent property of porphyrins are prone to be influenced by their aggregation status, which would attenuate the photodynamic antitumor efficiency (*35*). Therefore, ROS generation induced by siRNA/PPA-NG under irradiation was investigated using 2′,7′-dichlorodihydrofluorescein diacetate (DCFH-DA) as a fluorescent probe, which was hydrolyzed into DCFH by sodium hydroxide before the use. In the presence of ROS, nonfluorescent DCFH could be oxidized to DCF (*36*, *37*), which is highly fluorescent with the excitation/emission wavelengths of 488/522 nm. Upon illuminating the mixture of siRNA/PPA-NG and DCFH, the ROS generation was determined by recording the fluorescence intensity of DCF channel. As shown in Fig. 3D, the original siRNA/PPA-NG and DCFH have a low fluorescence intensity. After being exposed to a 660-nm laser irradiation with a photodensity of 100 mW/cm^2, the fluorescence intensity of mixture increased over the irradiation time, indicating that siRNA/PPA-NG could efficiently generate ROS under irradiation. To check whether the induced ROS damage the nearby siRNA in the system, 15% denaturing PAGE gel electrophoresis was conducted after exposing the nanogel under laser irradiation for different durations (0, 2, 5, and 10 min, respectively). As shown in fig. S6, compared to the bands of nanogel sample without irradiation (0 min), no obvious change could be found after irradiating the nanogel for 10 min, indicating that the produced ROS could not damage the nearby siRNA in our study. Besides ROS generation, the release of embedded siRNAs from siRNA/PPA-NG to play its functions is also a key step for synergistic photoimmunotherapy. It is well known that the ribonuclease H (RNase H) can recognize DNA/RNA hybrid duplex and specifically digest the RNA segment (*38*). Our nanogel assembly relies on the hybridization of sticky ends between tetrahedral framework and siRNA linkers, which forms DNA/RNA duplex. Hence, functional siRNA duplex would be released from the siRNA/PPA-NG in the presence of RNase H once the RNA overhangs are digested by the enzyme. As shown in Fig. 3E, released PD-L1 siRNA could be observed after incubating the nanogel with RNase H for 1 hour, which would down-regulate the target mRNA within tumor cells. With higher concentration of RNase H, more released siRNA could be found in the gel. Meanwhile, more disassembled PPA-DNA conjugates ran into the gel and appeared as sharp bands at the position slightly above the PS-modified DNA, revealing that the RNase H only digests the RNA segment of the DNA/RNA duplex (Fig. 3E).

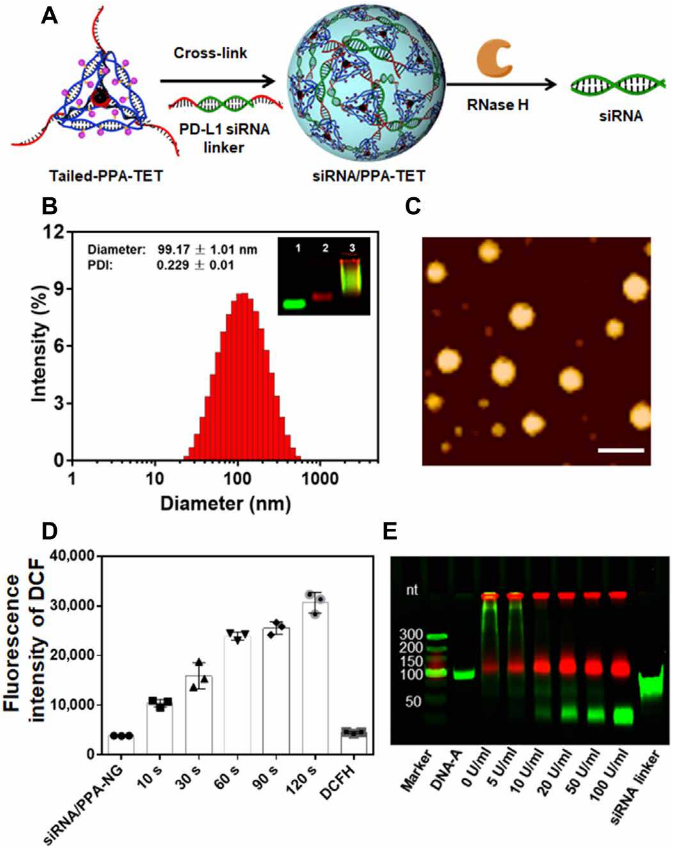

Fig. 3. Preparation and characterizations of siRNA/PPA-NG. (**A**) The schematic illustration of programmed self-assembly of siRNA/PPA-NG and RNase H–mediated siRNA release from nanogel. (**B**) Hydrodynamic diameter of the obtained nanogel under optimized condition. Inset: 1% agarose gel image containing siRNA linker (1), tailed-PPA-TET (2), and nanogel (3). PDI, polydispersity index. (**C**) The morphology of siRNA/PPA-NG revealed by AFM imaging. Scale bar, 500 nm. (**D**) The ROS generation induced by illuminating siRNA/PPA-NG under a 660-nm laser for different time (PPA concentration: 0.25 μM, 100 mW/cm^2). (**E**) 10% denaturing PAGE gel image of siRNA/PPA-NG after incubation with RNase H for 1.0 hour at 37°C. Green fluorescent bands represent unmodified component DNAs and siRNA linker, which are stained by EB. Red fluorescent bands indicate the PPA-grafted DNAs, which are imaged under a 650-nm channel.

Internalization of siRNA/PPA-NG into melanoma cells in vitro and in vivo

Following the successful preparation of siRNA/PPA-NG, we subsequently demonstrated the efficient internalization of siRNA/PPA-NG into B16-F10 melanoma cells, both in vitro and in vivo. For in vitro cellular uptake study, siRNA linker was labeled with 5-carboxyfluorescein (FAM) to track the nanogel inside the cells. The influence of incubating time and concentration of siRNA/PPA-NG on cellular uptake efficiency was evaluated by flow cytometry analysis (Fig. 4, A and B). Therefore, FAM-labeled siRNA linker and FAM-siRNA/PPA-NG (1.0 μM FAM) were incubated with B16-F10 cells for different durations (0.5, 1.0, 2.0, 4.0, and 6.0 hours) or at different nanogel concentrations (0.2, 0.5, 1.0, and 2.0 μM in terms of FAM) for 6 hours. As shown in Fig. 4, the FAM-siRNA/PPA-NG exhibits a time- and concentration-dependent cellular uptake behaviors. The nanogel-treated cells exhibited remarkably fluorescent signals after incubation, either barely for 0.5 hours at a concentration of 1.0 μM (in terms of FAM; Fig. 4A) or at a low concentration of 0.2 μM for 6 hours (Fig. 4B), which can be ascribed to its unique nanosized 3D architecture (*32*). In contrast, the linker alone can hardly enter to cells even incubated for 6 hours or at a concentration of 2.0 μM (fig. S7), as nucleic acid is a well-known negatively charged molecule. The same results were observed in the confocal laser scanning microscopy (CLSM) imaging. As shown in Fig. 4C, with longer incubation time, stronger fluorescent signals of both FAM and PPA could be observed, indicating the time-dependent cellular internalization of nanogel. Notably, the fluorescent signals from FAM channel and PPA channel are highly correlated based on Pearson correlation analysis of the CLSM images (fig. S8) and gradually decrease over the time, implying the rapid uptake of the entire nanogel and its progressive disassembly inside the cells.

To exploit the in vivo cellular uptake of nanogel and its accumulation in tumor cells, B16-F10 cell suspension was subcutaneously injected into the right flank of C57BL/6 mice to construct the melanoma mouse model. The melanoma tumor–bearing mice were intravenously administrated with Cy5.5-labeled nanogel when the tumor volume reached ~200 mm^3 and euthanized at 1, 12, and 24 hours after injection, respectively. Then, the tumor tissues were dissected and frozenly sectioned for CLSM imaging. As shown in Fig. 4D, strong PPA signals were observed in tumor cells even after 24 hours, revealing excellent penetration and accumulation of siRNA/PPA-NG at the tumor site.

In vitro antitumor effects induced by siRNA/PPA-NG

Because phototoxicity is majorly caused by ROS during the PDT treatment, ROS generation induced by siRNA/PPA-NG inside

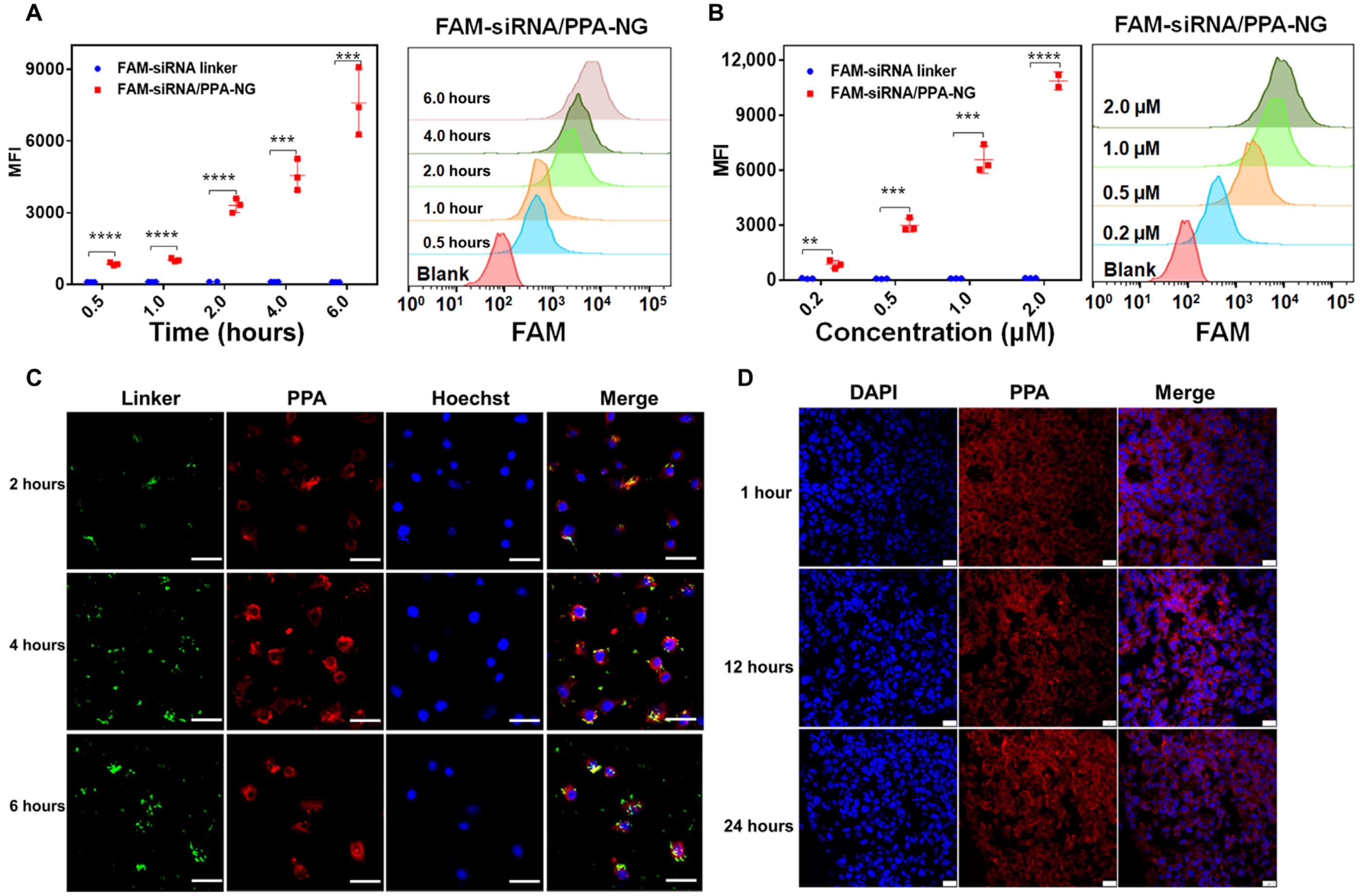

Fig. 4. Cellular uptake behaviors of siRNA/PPA-NG. (**A**) Flow cytometry results of FAM-labeled siRNA/PPA-NG and siRNA linker (1.0 μM FAM) after incubating with melanoma cells for different durations. (**B**) Flow cytometry analysis of melanoma cells incubated with FAM-labeled siRNA/PPA-NG and siRNA linker for 6 hours at different concentrations. MFI, mean fluorescence intensity. (**C**) CLSM images of melanoma cells after incubated with the siRNA/PPA-NG for different durations. Scale bars, 25 μm. (**D**) CLSM images of the tumor sections obtained from the mice at 1, 12, and 24 hours postinjection after intravenously administrating the siRNA/PPA-NG to mice. Scale bars, 25 μm.

melanoma cells was further evaluated under laser light irradiation. To facilitate the cell membrane penetration, again, DCFH-DA was chosen as ROS probe, which could be hydrolyzed into nonfluorescent DCFH inside the cell for ROS detection (*36*, *37*). After transfecting the B16-F10 cells with siRNA/PPA-NG for 6 hours and following the incubation with DCFH-DA containing Opti-MEM medium for another 30 min, B16-F10 cells were exposed under a 660-nm laser irradiation with a luminous intensity of 100 mW/cm^2 for 120 s. As shown in Fig. 5A, compared to nonilluminated cells, strong green fluorescence of DCF can be observed in the laser-treated group, indicating that our prepared nanogel can generate lots of ROS under laser irradiation. Meanwhile, the phototoxicity of siRNA/PPA-NG in vitro with or without irradiation was investigated by 3-(4,5-dimethylthiazol-2-yl)-2,5-diphenyltetrazolium bromide (MTT)–based cytotoxicity assay using free PPA solution as a control. For the groups without irradiation (Fig. 5C), siRNA/PPA-NG shows no cytotoxicity to B16-F10 cells, while the free PPA solution exhibits remarkably inhibited tumor cell proliferation even without the irradiation, revealing that packaging PPA in siRNA/PPA-NG greatly reduces its dark toxicity. It has been reported that the dark toxicity of photosensitizers is related with the interaction with Yes-associated protein, which is also dependent on the photosensitizer concentration in cells (*39*, *40*). Because of the protective 3D structure, the nanogel could inhibit the interactions between PPA and proteins in cytoplasm and reduce the effective concentration of free PPA inside cells, resulting in the reduced dark toxicity of photosensitizers. After being illuminated with laser light, siRNA/PPA-NG significantly induces cell death because of the ROS generation (Fig. 5D), indicating the excellent photodynamic efficacy of our nanogel. The calculated median inhibitory concentration (IC_{50}) of free PPA and siRNA/PPA-NG under irradiation was 0.05 and 0.25 μM, respectively. The free PPA exhibited lower IC_{50}, which can be ascribed to the addition of the dark toxicity and phototoxicity. Furthermore, to investigate whether the siRNA could be released from the nanogel and down-regulate PD-L1 checkpoint protein, Western blot assay was conducted to assess the PD-L1 expression using free siRNA and scramble siRNA cross-linked nanogel (SCR/PPA-NG) as control formulations. As shown in Fig. 5B, siRNA/PPA-NG can remarkably decrease the PD-L1 expression in melanoma cells compared to both free and scramble siRNA groups.

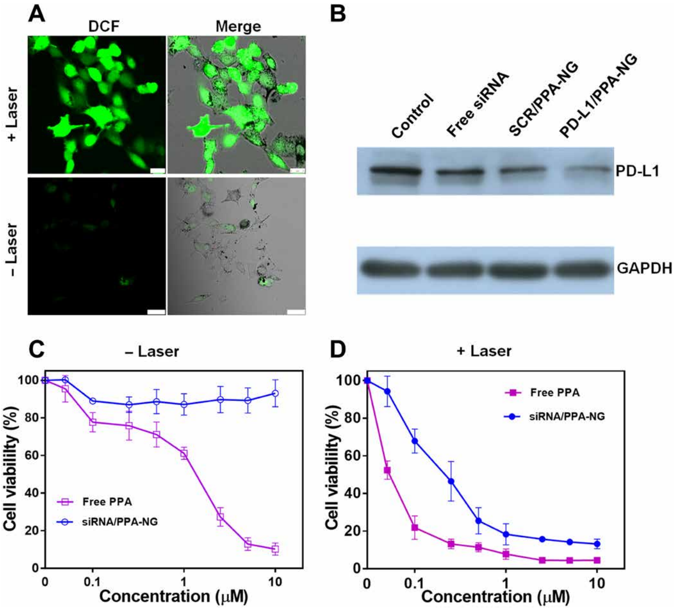

Fig. 5. In vitro antitumor capability of siRNA/PPA-NG. (**A**) CLSM images of siRNA/PPA-NG–treated B16-F10 cells with or without 660-nm laser light illumination (120 s) after incubating with DCFH-DA. Scale bars, 25 μm. (**B**) PD-L1 expression in B16-F10 cells after treatment with free siRNA, SCR/PPA-NG, and PD-L1/PPA-NG. GAPDH, glyceraldehyde-3-phosphate dehydrogenase. (**C**) Cytotoxicity of free PPA and siRNA/PPA-NG to B16-F10 cells without illumination. (**D**) Cytotoxicity of free PPA and siRNA/PPA-NG to B16-F10 cells after irradiating for 120 s under 660-nm laser light at photodensity of 100 mW/cm^2. The cell viability is calculated by cell viability (%) = $[(A_s - A_b)/(A_c - A_b)] \times 100\%$, wherein A_s is the absorbance of treated cells, A_c is the absorbance of blank cells without any treatment, and A_b is the absorbance of blank well.

In vivo synergistic antitumor immunity of siRNA/PPA-NG

It has established that PDT can induce ICD of the tumor cells and release TAAs, thereby resulting in an effective tumor-specific immune response (*41*). However, the immune response induced by PDT is usually too weak to kill the established tumors with immunosuppressive microenvironment (*42*, *43*) but prone to resulting in metastasis of tumors. Many malignancies overexpress the PD-L1 on the surface tumor cell membrane, which interacts with PD-1 receptors on antigen-stimulated T cells, inhibiting their killing capability of the target cells and cytokine secretion (*44*). Thus far, anti–PD-1/PD-L1 treatment has been widely applied to break the immunosuppressive blockade, which can significantly reactivate the immune system to inhibit the proliferation and metastasis of malignant tumors (*45*, *46*).

To evaluate the synergistic efficiency of photodynamic immunotherapy exerted by siRNA/PPA-NG, we established a melanoma-bearing mouse model using B16-F10 cells and investigated the immune response by monitoring the key immune cells through flow cytometry. When xenograft tumors reached to ~300 mm^3, mice were treated with different formulations, and subsequent experiments were conducted as depicted in fig. S9. The mice were randomly divided into four groups and administrated with phosphate-buffered saline (PBS), nanogel copackaged with PPA and PD-L1 siRNA with or without irradiation (abbreviated as PD-L1/PPA-NG + laser and PD-L1/PPA-NG − laser, respectively), and nanogel copackaged with PPA and scramble siRNA with irradiation (SCR/PPA-NG + laser), respectively. According to the previously reported mechanism, PDT-induced TAAs can be engulfed by immature DCs, resulting in DC maturation (*47*). Thereafter, mature DCs migrate to the tumor-draining lymph nodes and prime the TAAs to the T lymphocytes for activation. Thus, we dissected the inguinal lymph nodes of melanoma mice 3 days after being injected with different formulations (fig. S9) and collected the DCs. The frequencies of mature DCs were determined by flow cytometry after staining the cells with anti-CD11c, anti-CD80, and anti-CD86 antibodies. As shown in Fig. 6 (A and B), compared to PBS group (with 9.0 ± 4.8% mature DCs), PD-L1/PPA-NG − laser and SCR/PPA-NG + laser treatments can promote the frequency of mature DCs to 18.3 ± 1.6 and 17.9 ± 2.3% ($CD11c^+/CD80^+/CD86^+$), respectively. In contrast, PD-L1/PPA-NG + laser–treated group exhibits much higher maturation frequency of DCs (36.7 ± 5.8%), revealing that our nanogel-based PDT/ICB combinational therapy can significantly improve the TAA release and facilitate DC maturation compared to monotherapies.

Upon activation, CTLs ($CD3^+/CD8^+/CD4^-$) may infiltrate into tumor tissues and kill tumors cells by secreting toxic cytokines such

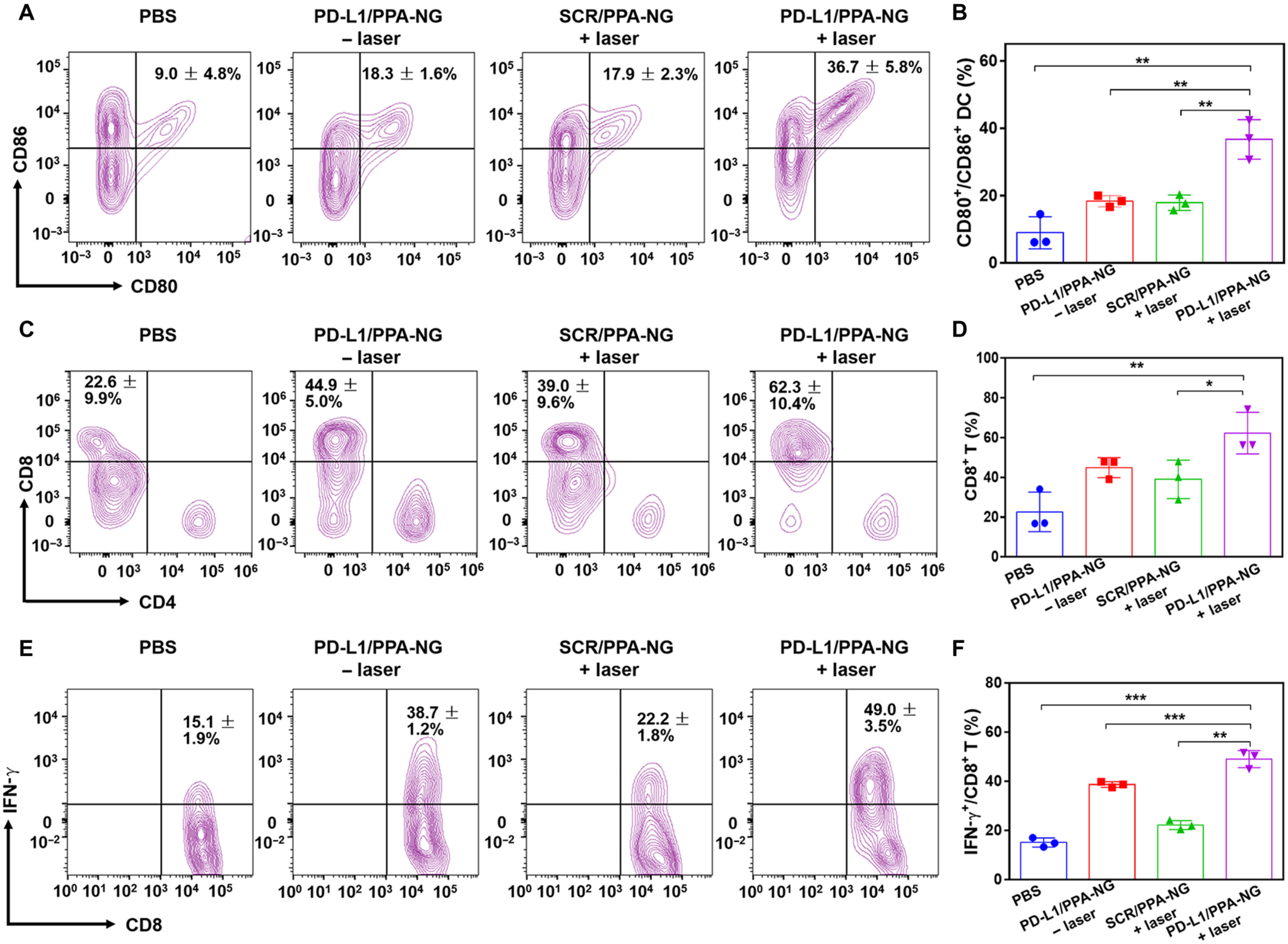

Fig. 6. In vivo synergistic antitumor immunity of siRNA/PPA-NG. (**A**) Flow cytometry examination of CD80$^+$/CD86$^+$ dual-positive DCs from the inguinal lymph nodes of the mice after the treatment with different formulations. (**B**) The summarized frequency of mature DCs (CD80$^+$/CD86$^+$) in all collected DCs after the treatment. (**C**) Flow cytometry examination of tumor-infiltrating CD8$^+$ T lymphocytes after the treatment with different formulations. (**D**) The summarized frequency of CD8$^+$ T lymphocytes in tumor. (**E**) Flow cytometry examination of CD8$^+$/IFN-γ$^+$ dual-positive effector T lymphocytes from dissected tumors after the treatment. (**F**) The summarized frequency IFN-γ–positive CD8$^+$ T lymphocytes in tumors after the treatment.

as perforin, granzyme, and interferon-γ (IFN-γ) (*48*). Therefore, we further collected lymphocytes from the tumor tissues and determined the infiltrating T cells by flow cytometry after staining the sample with anti-CD3, anti-CD4, and anti-CD8 antibodies (Fig. 6, C and D). In comparison with PBS-treated group, the frequency of CTL cells in PD-L1/PPA-NG – laser and SCR/PPA-NG + laser groups were increased to 44.9 ± 5.0 and 39.0 ± 9.6%, which are 1.98- and 1.73-fold higher than that of PBS group. Moreover, PD-L1/PPA-NG + laser group exhibits the highest CTL filtration in tumor tissues with a frequency of 62.3 ± 10.4%, which is 2.76-fold higher than that of PBS group. We also evaluated the IFN-γ expression in CD8$^+$ T cells by staining with corresponding antibodies (anti-CD3/anti-CD8/anti–IFN-γ; Fig. 6, E and F). Similarly, anti–PD-L1 and PDT treatment alone can promote the frequency of CD8$^+$/IFN-γ$^+$ dual-positive T cells to 38.7 ± 1.2 and 22.2 ± 1.8%, which is 2.56- and 1.47-fold higher compared with the PBS group. The synergistic treatment group shows the highest frequency (49.0 ± 3.5%) of CD8$^+$/IFN-γ$^+$ dual-positive T cells, which is 3.25-fold higher than that of PBS group. All above results demonstrate that our nanogel-based PDT/ICB combinational therapy can induce stronger immune response than monotherapy, implying its potential in enhancing the antitumor efficacy.

In vivo tumor inhibition using siRNA/PPA-NG

Last, in vivo tumor inhibition using PD-L1/PPA-NG was investigated on a bilateral tumor model following the protocol shown in fig. S10, in which the distant tumor (left flank tumor) was used to evaluate the efficacy of the systemic antitumor immune response. When the volume of primary tumor (right flank tumor) reached to ~100 mm^3, different drug formulations were intravenously injected with an equivalent concentration of PPA (5 mg/kg) every 2 days for three times. Following the procedure illustrated in fig. S10, primary tumors were irradiated under a 660-nm laser (100 mW/cm^2) for 10 min at 4 hours postinjection after each administration, while the distant tumors were not applied with any treatment. Tumor volumes were monitored for the whole process. As shown in Fig. 7A, the melanoma malignantly proliferates in nontreated group (PBS group) as demonstrated by rapidly increased volume of primary tumor. Monotherapies including PD-L1/PPA-NG − laser and SCR/PPA-NG + laser treatments can retard the tumor growth in some extent compared to PBS group. However, tumors still keep steady growing during the treatment with these two protocols. In contrast, synergistic therapy achieved by PD-L1/PPA-NG + laser exhibits the best antitumor efficiency in which the tumor proliferation is close to completely inhibited, giving a flatten curve regarding the tumor volume profile (Fig. 7A). After the treatment, dissected tumors were imaged, and their weights were recorded. As shown in Fig. 7 (B and C), tumors in the combinatorial therapy group are smallest both in size and weight compared to those in control groups. Above results indicate the excellent synergistic effect of our nanogel in antitumor therapy, which could be ascribed to the strong immune activation induced by the combinational PDT/ICB treatment (Fig. 6). The dissected primary tumors were further sliced and stained for pathological and immunofluorescence analysis (Fig. 7D). In hematoxylin and eosin (H&E) staining images, tumor in PD-L1/PPA-NG + laser group exhibits obvious cell shrinkage and nucleus condensation compared to those of monotherapy groups. The terminal deoxynucleotidyl transferase–mediated deoxyuridine triphosphate nick end labeling (TUNEL) assay further reveals the increased apoptosis of tumor cells after synergistic therapy, revealing a better antitumor efficiency. Furthermore, in vivo PD-L1 downregulation in tumor tissue was evaluated by immunohistochemical analysis and Western blot assay. As shown in Fig. 7 (E and F), PD-L1 expression in tumors is obviously reduced after the treatment, revealing its excellent in vivo gene silencing capability.

To verify the inhibition of distal tumors by PDT-stimulated immunity, volumes of distant tumors were also monitored during the treatment on primary tumors (Fig. 7G). Compared to PBS, PD-L1/PPA-NG − laser, and SCR/PPA-NG + laser groups, the distant

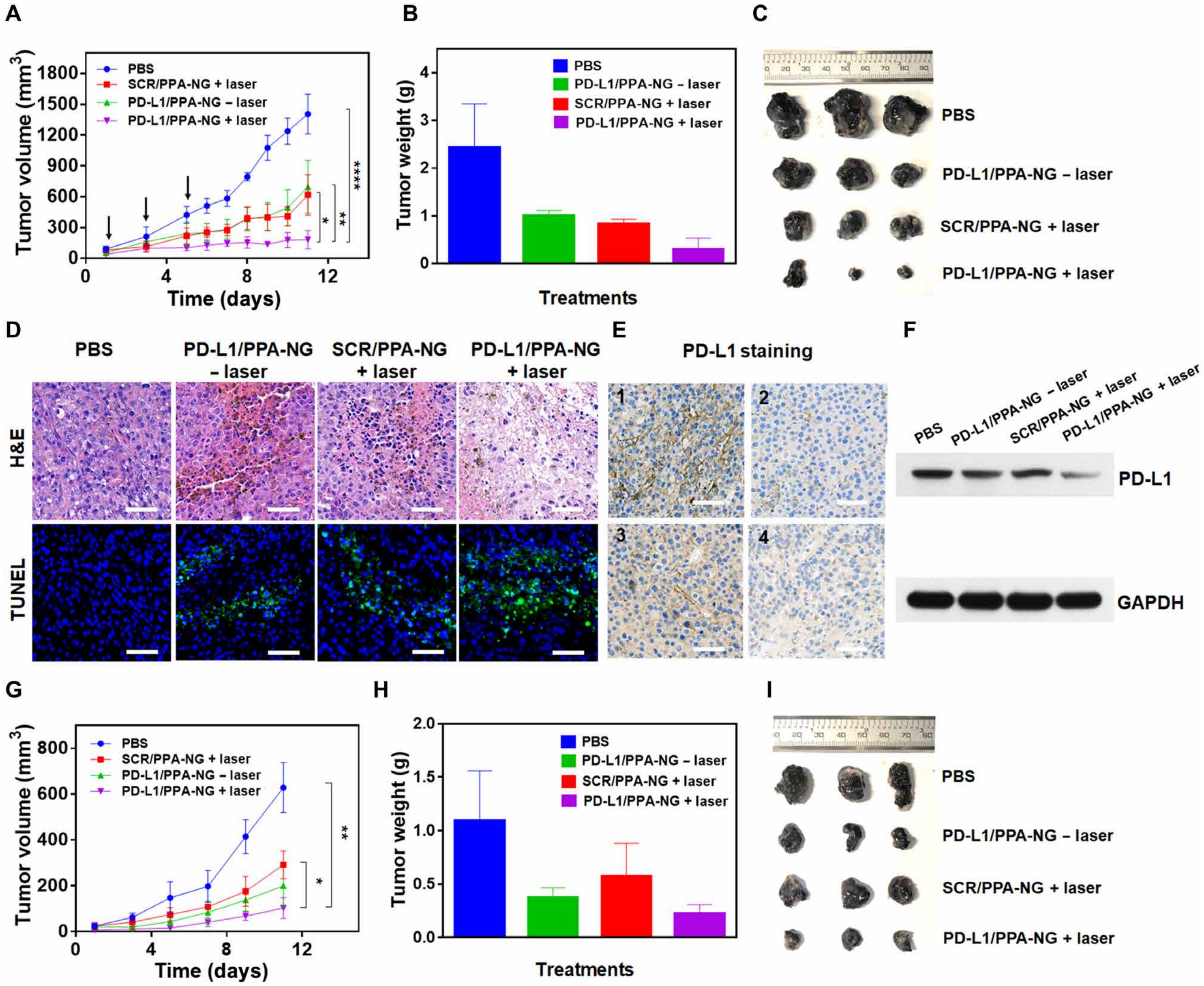

Fig. 7. In vivo tumor inhibition of PD-L1/PPA-NG in bilateral tumor-bearing mouse model. (**A**) Growth curve of the primary tumors during the treatment. (**B**) The final primary tumor weights in different groups after the treatment. (**C**) The images of dissected primary tumors after the treatment. (**D**) H&E staining and TUNEL analysis of the primary tumors treated with different formulations. (**E** and **F**) PD-L1 expression in the primary tumors determined by immunohistochemical and Western blot analysis. 1, PBS group; 2, PD-L1/PPA-NG − laser group; 3, SCR/PPA-NG + laser group; 4, PD-L1/PPA-NG + laser group. (**G** to **I**) Growth curves, weights, and images of the distant tumors during the treatment. Scale bars, 50 μm.

tumors in PD-L1/PPA-NG + laser group show the slowest proliferation. After the treatment, distant tumors were also dissected and weighted (Fig. 7, H and I). Similar to the primary tumor scenario, PD-L1/PPA-NG + laser–treated group shows the best tumor inhibition effect, as evidenced by the lowest volumes and weights of distant tumors after the treatment. This result confirms that strong antitumor immune response can be triggered by the nanogel-based synergistic photodynamic immunotherapy.

In vivo biosafety assessment

Furthermore, the biosafety of the nanogel was evaluated by collecting the main tissues (heart, liver, spleen, lung, and kidney) after different treatment and analyzed by H&E staining. As shown in fig. S11, the heart, liver, spleen, lung, and kidney in treated groups demonstrate no distinguishable change compared with the control mice, indicating the good biosafety and biocompatibility of our nanogel. Moreover, the serum biochemistry assays were further conducted using healthy C57BL/6 mice to evaluate the influence of nanogel materials on the liver and kidneys' functions. After the mice were intravenously injected with PD-L1/PPA-NG every 2 days for three times at a PPA dosage of 5 mg/kg, serums were harvested to detect the liver- and kidney-related biochemical indexes. As shown in fig. S12, compared with the control group, the nanogel-treated mice show a similar level of alanine aminotransferase, aspartate aminotransferase, blood urea nitrogen, and creatinine, indicating that the functions of liver and kidneys were not affected by the treatment. All results above confirmed the excellent biocompatibility of the nanogel for synergistic antitumor treatment.

DISCUSSION

In this study, we simply introduced the phosphorothioate modifications on DNA backbone and make them as anchor sites to directly graft multiple PPA photosensitizers on DNA strands. With the synthesized PPA-grafted DNAs, a tetrahedral DNA framework with a sticky end at each vertex was successfully engineered, which was used as structural units to assemble with PD-L1 siRNA linkers to form an siRNA- and PPA-bearing nanogel for synergistic photodynamic immunotherapy. In this way, photosensitizer and functional siRNA were conveniently packaged in a nanogel carrier through nucleic acid self-assembly. Compared to other conjugation strategy, direct grafting photosensitizer on DNA can avoid the use of any other exogenous carrier materials, and the PS-based drug grafting provides a facile way to prepare DNA drug conjugates with good controllability. As shown in our study, multitude of interested drug molecules can be easily and quantitatively grafted onto DNA strands, enabling the precise control over the drug loading ratio. By tuning the positions of PS modification on component DNA strands, the prepared PPA-DNA conjugates could retain the water solubility and Watson-Crick base pairing property, which enables the self-assembly of tailed-PPA-TET building blocks and final siRNA/PPA-bearing nanogels. Overall, the siRNA/PPA-NG assembly is simple and can be readily achieved by mixing PD-L1 siRNA linker and tailed-PPA-TET. With established knowledge on DNA self-assembly, we can also modulate the size of this nanogel by regulating the ratio of siRNA linker and TET. It is worth to mention that grafting PPA onto DNA strands can greatly enhance its aqueous solubility. After conjugation, the hydrophilic DNA assist the PPA homogeneously dissolve in buffer solution rather than aggregating together to form a micelle, which promotes the quantum yield of ROS production and photodynamic efficacy. In addition, the cross-linking strategy using functional siRNA as linkers protected the siRNA from degradation by enzymes, leading to efficient gene silencing and knockdown of immune checkpoints. As a result, the prepared siRNA/PPA-NG induced the strongest immune response and excellent tumor inhibition efficiency. In future, our multidrug copackaged nanogel can be easily expanded to a wide range of synergistic formulations by replacing the photosensitizer into other types of small-molecule drugs. Meanwhile, the siRNA linkers could also be facilely altered into sequences that down-regulate other targets of interests or other types of functional nucleic acids, such as microRNAs. Besides cancer treatment, this nanogel could be modified with targeting moieties or applied for local delivery to achieve better therapeutic efficacy in different indications. In summary, this study presents a noncationic nanoplatform for simultaneous delivery of ICB and PDT agents with good biosafety, excellent photodynamic efficiency, promoted immune response, effective tumor inhibition, and anti-metastasis efficiency, which may become as a promising strategy to construct new types of nanomedicine for combinatorial cancer immunotherapy.

MATERIALS AND METHODS

Materials

4-Dimethylaminopyridine (DMAP), *N*,*N*-dicyclohexylcarbodiimide (DCC), *N*,*N*,*N*,*N*-tetramethylethylenediamine, ammonium persulfate, DMSO, dichloromethane (DCM), ethidium bromide (EB), and acetonitrile were purchased from Adamas-beta (China). (4-(Bromo methyl)phenyl)methanol was purchased from Shanghai BiDe Pharmaceutical Technology Co. Ltd. (China). PPA was obtained from Shanghai Dibai Biological Technology Co. Ltd. (China). Acrylamide/bis-acrylamide solution was purchased from Sangon Biotech Co. Ltd. (China). Dulbecco's modified Eagle medium (DMEM) was obtained from Gibco (USA). Fetal bovine serum was purchased from PAA Laboratories GmbH (Austria). Tris, EDTA, magnesium acetate tetrahydrate, and acetic acid were purchased from Macklin Reagent (China). Paraformaldehyde was purchased from Sinopharm Chemical Reagent Co. Ltd. (China). Agarose, thiazolyl blue tetrazolium bromide (MTT), and fluoromount aqueous mounting medium were purchased from Sigma-Aldrich (USA). Hoechst 33342 was obtained from Invitrogen (USA). ROS detection kit (DCFH-DA) was purchased from Beyotime Biotechnology Co. Ltd. (China). Antibodies for lymphocytes detection and Fix/Perm reagent were purchased from BD Biosciences (USA). Deoxyribonuclease I from bovine pancreas, collagenase IV, hyaluronidase, and red blood cell lysis buffer were purchased from Shanghai Yeasen BioTechnologies Co. Ltd. (China). Mouse lymphocyte separation fluid was purchased from Dakewe (China). Clear polystyrene tissue culture treated with 24- and 96-well plates were obtained from Corning Costar (USA). All the DNA and RNA strands were obtained from Shanghai DNA Bioscience Co. Ltd. (China). The siRNAs used in this study are not chemically modified.

Synthesis of PPA-Bz-Br

A total of 200 mg of PPA [1.1 equivalent (eq.)] and 67.5 mg of (4-(bromo methyl)phenyl)methanol (1.0 eq.) were dissolved in dry DCM. Then, DMAP (0.3 eq.) was added during stirring. Afterward, DCC (1.2 eq.) dissolved in dry DCM was dropwisely added into the mixed solution under ice bath condition. Thin layer chromatography was used to monitor the reaction under DCM/methanol as mobile phase. After completely reacting, the crude products were purified by silica gel column chromatography to obtain the pure PPA-Bz-Br. The structure of PPA-Bz-Br was characterized by ^{1}H-NMR and ^{13}C-NMR. MS: 717.24/719.24, $[M + H]^+$. Yield: 43.6%.

Synthesis of PPA-phosphorothioate DNA conjugates (PPA-DNAs)

Ten OD (optical density) PS-DNAs in a 2.0-ml Eppendorf tube were dried by a rotary evaporator. PPA-Bz-Br dissolved in DMSO (30 mM) was added into the DNA powder to obtain mixture with the final DNA concentration of 200 μM. The mixture was vibrated at 55°C for 1 hour. After reaction, 200 μl of 10× elusion buffer (5 M ammonium acetate, 0.1 M magnesium acetate tetrahydrate, and 0.02 M EDTA) and 1.8 ml of ethyl alcohol were added into the mixture for overnight at −80°C. The mixture was centrifuged under 12000 rpm for 20 min at 4°C, and the supernatant was removed. The obtained precipitates were washed by DCM/ethyl alcohol (1:1) solution for six times. The final product was obtained after dried under a rotary evaporator. The obtained PPA-DNA conjugates were characterized by 15% denaturing PAGE gel (15% acrylamide solution containing 8.3 M urea) after dissolved in TBE buffer (89 mM tris, 89 mM boric acid, and 2 mM EDTA; the pH was adjusted to 7.4). The molecule weight of a representative PPA-DNA conjugate was determined on a Shimadzu MALDI 7090 TOF-TOF MS (Shimadzu Corporation, Japan). Detection conditions are as follows: liner model; laser diameter, 200 μm; power, 167; matrix, 3-hydroxypicolinic acid.

Determination of PPA content

UV spectroscopy was used to determine the content of PPA. First, PPA was dissolved in acetonitrile with a concentration range from 0.1 to 25.0 μg/ml (fig. S3). The UV/vis spectra and absorbance at 667 nm were recorded to derive the standard curve by linear regression using the absorbance. Then, the absorbance at 667 nm of PPA-DNA conjugates were recorded after dissolved in acetonitrile to calculate the concentration of PPA. The drug content could be readily calculated by determining the DNA absorbance at 260 nm at the same time.

Preparation of PPA-bearing DNA tetrahedral framework (tailed-PPA-TET)

Equal molar of the four PPA-grafted DNA strands were mixed in TAE/Mg^{2+} buffer and incubated at 95°C for 5 min. Later on, the mixture solution was transferred to 4°C condition immediately to obtain the tailed-PPA-TET. Four percent PAGE gel and 2% agarose gel were used to characterize the successful assembly of the PPA-bearing DNA tetrahedral framework under native condition (1× TAE/Mg^{2+} buffer solution).

Preparation of siRNA/PPA-NG

To obtain the siRNA/PPA-NG, the siRNA linker was prepared by mixing the sense and antisense strand at equal molar ratio in TAE/Mg^{2+} buffer (diethyl pyrocarbonate water). The mixture was heated to 85°C for 10 min, followed by natural annealing to room temperature. Thereafter, the siRNA/PPA-NG was readily achieved by mixing the siRNA linker and tailed-PPA-TET. The assembly condition was optimized by mixing tailed-PPA-TET and siRNA linker at a ratio range from 1:0.5 to 1:2.5. The successful assembly of the nanogel was characterized by 4% PAGE (fig. S5A) and 0.5% agarose gel electrophoresis (fig. S5B) under native condition.

DLS analysis of siRNA/PPA-NG

The DLS analysis of siRNA/PPA-NG was conducted on a Zetasizer Nano ZS instrument (Malvern Instruments, UK) equipped with a 125-mW laser at 25°C. The scattering angle was kept at 173°, and the wavelength of laser light was 633 nm during the whole experiment.

AFM imaging of siRNA/PPA-NG

Five microliters of siRNA/PPA-NG was spotted onto a mica surface and incubated for 5 min to ensure that the nanogel absorbed on the substrate. Then, 10 μl of pure water was added to wash off and dried by compressed air. The morphology of the nanogel was observed under Nanonavi E-Sweep instrument (Japan).

RNase H–mediated siRNA release

The siRNA/PPA-NG was incubated with different concentrations of RNase H (0, 5, 10, 20, 50, and 100 U/ml) at 37°C for 1 hour. The release of functional RNA segments was characterized by 10% denaturing PAGE electrophoresis. After gel electrophoresis, gel images were recorded under Bio-Rad imaging system (USA).

ROS generation induced by siRNA/PPA-NG

DCFH was used as probe to determine the ROS generation in ex vivo condition. First, the DCFH was obtained by hydrolyzing the DCFH-DA (*49*, *50*). A total of 400 μl of sodium hydroxide solution (10.0 mM) was added into 100 μl of DCFH-DA (1.0 mM; diluted with methanol) and incubated for 30 min. The DCFH solution (40.0 μM) was obtained by adding 2.0 ml of sodium dihydrogen phosphate (25.0 mM) into the above mixture. Next, the siRNA/PPA-NG and DCFH were mixed, and the concentration of PPA and DCFH was adjusted to 0.25 μM and 1.0 μM, respectively. A 660-nm laser was used to directly illuminate the mixture at an intensity of 100 mW/cm^2 for different time intervals (10, 30, 60, 90, and 120 s). Then, the fluorescence intensity of DCF was determined on a microplate reader (Synergy H4, BioTek, USA) with the excitation/emission wavelengths of 488/522 nm.

Cell culture

B16-F10 cells were incubated in DMEM culture media containing 10% fetal bovine serum, penicillin (50 U/ml), and streptomycin (50 U/ml) at 37°C in a humidified atmosphere containing 5% carbon dioxide.

In vitro cell uptake by flow cytometry

B16-F10 cells were seeded in a 24-well plate at a density of 5×10^4 cells per well and cultured in DMEM for overnight. The FAM-labeled siRNA linker and nanogel were added into the wells with equal FAM concentration (1.0 μM) and incubated in Opti-MEM at 37°C for different time intervals (0.5, 1.0, 2.0, 4.0, and 6.0 hours) or with different concentrations of FAM (0.2, 0.5, 1.0, and 2.0 μM) and incubated for 6 hours. Cells were harvested and collected for flow cytometry analysis.

CLSM imaging

B16-F10 cells were seeded in a 24-well plate with a clean coverslip at the bottom at a density of 5×10^4 cells per well and cultured in

DMEM for overnight. FAM-siRNA linker and FAM-siRNA/PPA-NG were added with the FAM concentration of 1.0 μM and incubated in Opti-MEM for different time intervals (2.0, 4.0, and 6.0 hours). Then, the Opti-MEM was removed, and cells were rinsed three times with PBS solution, followed by addition of 4% formaldehyde to fix the cells for 20 min at room temperature. After removing the formaldehyde, the cells were rinsed three times by PBS. Later on, Hoechst 33342 was added to stain cell nucleus for 10 min. After rinsing with PBS, the slides were mounted and visualized under a CLSM (Leica TCS SP8 STED 3X, Germany).

In vitro cytotoxicity assay

Cells were seeded in 96-well plates with a density of 0.8×10^4 cells per well and incubated overnight, followed by replacing the medium to Opti-MEM and addition of free PPA solution (using DMSO as solubilizer) and siRNA/PPA-NG with a PPA concentration range from 0.05 to 10.0 μM. After 12 hours of incubation, the cells were illuminated under a 660-nm laser at an intensity of 100 mW/cm^2 for 150 s and sequentially incubated in DMEM medium for another 12 hours. Twenty microliters of MTT solution (5 mg/ml) was added into each well and incubated at 37°C for 4 hours, followed by removing the medium and addition of 150 μl of DMSO to dissolve formazan. The absorbance at 490 nm was recorded on a microplate reader (Synergy H4, BioTek, USA) to calculate the cell viability. Cells without illumination were used as control group to monitor the dark cytotoxicity of PPA.

PD-L1 down-regulation by siRNA/PPA-NG

B16-F10 cells were seeded in a six-well plate with a cell density of 1×10^5 cells per well and incubated in DMEM overnight, followed by replacing medium to Opti-MEM. The PD-L1 siRNA, scramble siRNA-bearing nanogel (SCR/PPA-NG), and PD-L1 siRNA-bearing nanogel (PD-L1/PPA-NG) were added with an siRNA concentration of 150 nM. After 24 hours, DMEM was added and incubated for another 24 hours. The total protein was extracted for Western blot analysis. The PD-L1 expression was imaged under electrochemical luminescence (Invitrogen).

Intracellular ROS generation

B16-F10 cells were seeded in 24-well plate with a clean coverslip at the bottom with a density of 5×10^4 cells per well and incubated overnight, followed by addition of siRNA/PPA-NG with a PPA concentration of 0.5 μM. After incubation for 6 hours, the supernatant was removed and replaced with fresh Opti-MEM containing 5.0 μM DCFH-DA for another 30 min. The supernatant was replaced into fresh medium, and cells were illuminated with a 660-nm laser light at an intensity of 100 mW/cm^2 for 120 s. Cells without illumination were used as control group. The treated cells were mounted after fixing by formaldehyde for further CLSM imaging.

Animals

All animal experiments were conducted under the Guide for the Care and Use of Laboratory Animals, and all operations were approved by the Animal Ethics Committee of Shanghai Jiao Tong University (A2019090). All experiments involving animals were performed in accordance with the guidelines of the Institutional Animal Care and Use Committee of Shanghai Jiao Tong University (China). Six- to 7-week-old C57BL/6 female mice were used in this study.

In vivo tumor accumulation of siRNA/PPA-NG

B16-F10 cells (5×10^5) were subcutaneously injected into the right flanks of C57BL/6 mice. As the tumor volume reached to around 200 mm^3, mice were intravenously administrated with Cy5.5-labeled siRNA/PPA-NG with a dosage of 5 mg of PPA per kilogram mouse. Mice were euthanized after 1, 12, and 24 hours, respectively. Then, tumor tissues were dissected and made into frozen section, followed by staining the nucleus with 4′,6-diamidino-2-phenylindole (DAPI). PPA and DAPI signals were observed by CLSM imaging.

In vivo immunological evaluation of siRNA/PPA-NG

B16-F10 cells (5×10^5) were subcutaneously injected into the right flanks of C57BL/6 mice. As the tumor volume reached around 300 mm^3, mice were intravenously administrated with different drug formulations with a dosage of 5 mg of PPA per kilogram mouse and 1 mg of siRNA per kilogram mouse. The mice were randomly divided into four groups for different treatment: 1, PBS group; 2, PD-L1/PPA-NG − laser group; 3, SCR/PPA-NG + laser group; 4, PD-L1/PPA-NG + laser group. Mice in the third and fourth groups were selectively irradiated by a 660-nm laser 4 and 24 hours after injection for 5 min at an intensity of 100 mW/cm^2. For irradiation operation, the hairs in tumor site were first shaved after anesthetizing the mice, followed with direct irradiation of the whole tumor with the 660-nm laser light. Each treatment was performed in triplicate. On the third day after administration, the mice were euthanized, and the inguinal lymph nodes and tumor tissues were dissected for immunological evaluation. To investigate the DC maturation frequency, DCs were harvested from the lymph nodes and stained with anti–CD11c-FITC (fluorescein isothiocyanate), anti–CD80-PE (phycoerythrin), and anti–CD86-PE-Cy7 (PE and cyanine 7 tandem dye) antibodies. The frequency of the CD11c$^+$/CD80$^+$/CD86$^+$ DC was detected by flow cytometry. For the tumor-infiltrating lymphocytes investigation, the dissected tumor tissues were cut into small pieces and digested in DMEM medium containing collagenase IV, hyaluronidase, and deoxyribonuclease at 37°C for 2 hours. A 75-μm cell mesh was used to obtain cell suspension, and the lymphocytes were isolated using mouse lymphocyte separation medium according to protocols. The collected lymphocytes suspensions were blocked with anti–CD3-FITC, anti–CD4-APC (allophycocyanin), and anti–CD8-PE-Cy7 antibodies at 4°C for 30 min for flow cytometry analysis. For IFN-γ$^+$/CD8$^+$ T cell analysis, the harvested lymphocyte suspensions were blocked with fluorescence-labeled anti–CD3-FITC and anti–CD8-PE-Cy7 antibodies, followed by permeabilization in Perm/Wash buffer (BD Biosciences, USA) for 30 min and stained with anti–IFN-γ–PE antibodies.

In vivo antitumor studies

Bilateral tumor model was established for in vivo antitumor studies. B16-F10 cells (5×10^5) were subcutaneously injected into right flanks of C57BL/6 mice to create primary tumor; 1×10^5 cells were subcutaneously injected into left flanks to create distant tumor. As the primary tumor volume reached to ~100 mm^3, the mice were randomly divided into four groups and intravenously injected with different drug formulations with an immobilized PPA and siRNA dosage of 5 and 1 mg/kg, respectively. The mice in the divided four groups undergone different treatment: 1, PBS; 2, PD-L1/PPA-NG − laser; 3, SCR/PPA-NG + laser; 4, PD-L1/PPA-NG + laser. The mice in the third and fourth groups were selectively irradiated on primary tumors by a 660-nm laser 4 hours after injection (100 mW/cm^2, 10 min). The treatments were repeated every 2 days for three times. The weights and tumor volumes were recorded. Mice were euthanized on day 12 for pathologic and immunohistochemical evaluation.

Statistical analysis

Data were presented as means ± SD. The statistical significance was determined using the analysis of variance and two-tailed Student's *t* test. Statistical significance was noted as follows: $*P < 0.05$; $**P < 0.01$; $***P < 0.001$; $****P < 0.0001$.

SUPPLEMENTARY MATERIALS

Supplementary material for this article is available at https://science.org/doi/10.1126/sciadv.abn2941

View/request a protocol for this paper from *Bio-protocol*.

REFERENCES AND NOTES

1. X. J. Jiang, J. Wang, X. Y. Deng, F. Xiong, J. S. Ge, B. Xiang, X. Wu, J. Ma, M. Zhou, X. L. Li, Y. Li, G. Y. Li, W. Xiong, C. Guo, Z. Y. Zeng, Role of the tumor microenvironment in PD-L1/PD-1-mediated tumor immune escape. *Mol. Cancer* **18**, 10 (2019).
2. M. Binnewies, E. W. Roberts, K. Kersten, V. Chan, D. F. Fearon, M. Merad, L. M. Coussens, D. I. Gabrilovich, S. Ostrand-Rosenberg, C. C. Hedrick, R. H. Vonderheide, M. J. Pittet, R. K. Jain, W. Zou, T. K. Howcroft, E. C. Woodhouse, R. A. Weinberg, M. F. Krummel, Understanding the tumor immune microenvironment (TIME) for effective therapy. *Nat. Med.* **24**, 541–550 (2018).
3. G. T. Motz, G. Coukos, Deciphering and reversing tumor immune suppression. *Immunity* **39**, 61–73 (2013).
4. A. Salmaninejad, S. F. Valilou, A. G. Shabgah, S. Aslani, M. Alimardani, A. Pasdar, A. Sahebkar, PD-1/PD-L1 pathway: Basic biology and role in cancer immunotherapy. *J. Cell. Physiol.* **234**, 16824–16837 (2019).
5. H. T. Lee, S. H. Lee, Y. S. Heo, Molecular interactions of antibody drugs targeting PD-1, PD-L1, and CTLA-4 in immuno-oncology. *Molecules* **24**, 1190 (2019).
6. W. Hugo, J. M. Zaretsky, L. Sun, C. Song, B. H. Moreno, S. Hu-Lieskovan, B. Berent-Maoz, J. Pang, B. Chmielowski, G. Cherry, E. Seja, S. Lomeli, X. Kong, M. C. Kelley, J. A. Sosman, D. B. Johnson, A. Ribas, R. S. Lo, Genomic and transcriptomic features of response to anti-PD-1 therapy in metastatic melanoma. *Cell* **165**, 35–44 (2016).
7. L. Luo, C. Zhu, H. Yin, M. Jiang, J. Zhang, B. Qin, Z. Luo, X. Yuan, J. Yang, W. Li, Y. Du, J. You, Laser immunotherapy in combination with perdurable PD-1 blocking for the treatment of metastatic tumors. *ACS Nano* **12**, 7647–7662 (2018).
8. D. E. Dolmans, D. Fukumura, R. K. Jain, Photodynamic therapy for cancer. *Nat. Rev. Cancer* **3**, 380–387 (2003).
9. M. H. Cho, Y. Li, P. C. Lo, H. Lee, Y. Choi, Fucoidan-based theranostic nanogel for enhancing imaging and photodynamic therapy of cancer. *Nano-Micro Lett.* **12**, 47 (2020).
10. L. Milla Sanabria, M. E. Rodriguez, I. S. Cogno, N. B. Rumie Vittar, M. F. Pansa, M. J. Lamberti, V. A. Rivarola, Direct and indirect photodynamic therapy effects on the cellular and molecular components of the tumor microenvironment. *Biochim. Biophys. Acta* **1835**, 36–45 (2013).
11. L. Galluzzi, A. Buqué, O. Kepp, L. Zitvogel, G. Kroemer, Immunogenic cell death in cancer and infectious disease. *Nat. Rev. Immunol.* **17**, 97–111 (2017).
12. W. Zou, Immunosuppressive networks in the tumour environment and their therapeutic relevance. *Nat. Rev. Cancer* **5**, 263–274 (2005).
13. D. Wang, T. Wang, J. Liu, H. Yu, S. Jiao, B. Feng, F. Zhou, Y. Fu, Q. Yin, P. Zhang, Z. Zhang, Z. Zhou, Y. Li, Acid-activatable versatile micelleplexes for PD-L1 blockade enhanced cancer photodynamic immunotherapy. *Nano Lett.* **16**, 5503–5513 (2016).
14. X. Duan, C. Chan, N. Guo, W. Han, R. R. Weichselbaum, W. Lin, Photodynamic therapy mediated by nontoxic core–shell nanoparticles synergizes with immune checkpoint blockade to elicit antitumor immunity and antimetastatic effect on breast cancer. *J. Am. Chem. Soc.* **138**, 16686–16695 (2016).
15. J. Xu, L. Xu, C. Wang, R. Yang, Q. Zhuang, X. Han, Z. Dong, W. Zhu, R. Peng, Near-infrared-triggered photodynamic therapy with multitasking upconversion nanoparticles in combination with checkpoint blockade for immunotherapy of colorectal cancer. *ACS Nano* **11**, 4463–4474 (2017).
16. L. Hu, Z. L. Cao, L. Ma, Z. Liu, G. Liao, J. Wang, S. Shen, D. Li, X. Yang, The potentiated checkpoint blockade immunotherapy by ROS-responsive nanocarrier-mediated cascade chemo-photodynamic therapy. *Biomaterials* **223**, 119469 (2019).
17. Y. Liu, J. Yang, B. Liu, W. Cao, J. Zhang, Y. Yang, L. Ma, J. M. de la Fuente, J. Song, J. Ni, C. Zhang, D. Cui, Human iPS cells loaded with MnO_2-based nanoprobes for photodynamic and simultaneous enhanced immunotherapy against cancer. *Nano-Micro Lett.* **12**, 127 (2020).
18. G. Lan, K. Ni, Z. Xu, S. S. Veroneau, Y. Song, W. Lin, Nanoscale metal-organic framework overcomes hypoxia for photodynamic therapy primed cancer immunotherapy. *J. Am. Chem. Soc.* **140**, 5670–5673 (2018).
19. C. W. Ng, J. C. Li, K. Y. Pu, Recent progresses in phototherapy-synergized cancer immunotherapy. *Adv. Funct. Mater.* **28**, 1804688 (2018).
20. T. K. Chen, Q. Li, Z. L. Liu, Y. Chen, F. Feng, H. P. Sun, Peptide-based and small synthetic molecule inhibitors on PD-1/PD-L1 pathway: A new choice for immunotherapy? *Eur. J. Med. Chem.* **161**, 378–398 (2019).
21. X. Han, L. Wang, T. Li, J. Zhang, D. Zhang, J. Li, Y. Xia, Y. Liu, W. Tan, Beyond blocking: Engineering RNAi-mediated targeted immune checkpoint nanoblocker enables T-cell-independent cancer treatment. *ACS Nano* **14**, 17524–17534 (2020).
22. B. Yoo, V. C. Jordan, P. Sheedy, A. M. Billig, A. Ross, P. Pantazopoulos, Z. Medarova, RNAi-mediated PD-L1 inhibition for pancreatic cancer immunotherapy. *Sci. Rep.* **9**, 4712 (2019).
23. P. Y. Teo, C. Yang, L. M. Whilding, A. C. Parente-Pereira, J. Maher, A. J. T. George, J. L. Hedrick, Y. Y. Yang, S. Ghaem-Maghami, Ovarian cancer immunotherapy using PD-L1 siRNA targeted delivery from folic acid-functionalized polyethylenimine: Strategies to enhance T cell killing. *Adv. Healthc. Mater.* **4**, 1180–1189 (2015).
24. L. Borkner, A. Kaiser, W. van de Kasteele, R. Andreesen, A. Mackensen, J. B. Haanen, T. N. Schumacher, C. Blank, RNA interference targeting programmed death receptor-1 improves immune functions of tumor-specific T cells. *Cancer Immunol. Immunother.* **59**, 1173–1183 (2010).
25. J. Soutschek, A. Akinc, B. Bramlage, K. Charisse, R. Constien, M. Donoghue, S. Elbashir, A. Geick, P. Hadwiger, J. Harborth, M. John, V. Kesavan, G. Lavine, R. K. Pandey, T. Racie, K. G. Rajeev, I. Rohl, I. Toudjarska, G. Wang, S. Wuschko, D. Bumcrot, V. Koteliansky, S. Limmer, M. Manoharan, H. P. Vornlocher, Therapeutic silencing of an endogenous gene by systemic administration of modified siRNAs. *Nature* **432**, 173–178 (2004).
26. S. M. Moghimi, P. Symonds, J. C. Murray, A. C. Hunter, G. Debska, A. Szewczyk, A two-stage poly(ethylenimine)-mediated cytotoxicity: Implications for gene transfer/therapy. *Mol. Ther.* **11**, 990–995 (2005).
27. K. J. Kauffman, M. J. Webber, D. G. Anderson, Materials for non-viral intracellular delivery of messenger RNA therapeutics. *J. Control. Release* **240**, 227–234 (2016).
28. Q. Hu, H. Li, L. Wang, H. Gu, C. Fan, DNA nanotechnology-enabled drug delivery systems. *Chem. Rev.* **119**, 6459–6506 (2019).
29. M. Zheng, T. Jiang, W. Yang, Y. Zou, H. Wu, X. Liu, F. Zhu, R. Qian, D. Ling, K. McDonald, J. Shi, B. Shi, The siRNAsome: A cation-free and versatile nanostructure for siRNA and drug co-delivery. *Angew Chem. Int. Edit* **58**, 4938–4942 (2019).
30. X. Y. Tan, X. G. Lu, F. Jia, X. F. Liu, Y. H. Sun, J. K. Logan, K. Zhang, Blurring the role of oligonucleotides: Spherical nucleic acids as a drug delivery vehicle. *J. Am. Chem. Soc.* **138**, 10834–10837 (2016).
31. Y. Y. Guo, J. Zhang, F. Ding, G. F. Pan, J. Li, J. Feng, X. Y. Zhu, C. Zhang, Stressing the role of DNA as a drug carrier: Synthesis of DNA-drug conjugates through grafting chemotherapeutics onto phosphorothioate oligonucleotides. *Adv. Mater.* **31**, e1807533 (2019).
32. H. Xue, F. Ding, J. Zhang, Y. Y. Guo, X. H. Gao, J. Feng, X. Y. Zhu, C. Zhang, DNA tetrahedron-based nanogels for siRNA delivery and gene silencing. *Chem. Commun.* **55**, 4222–4225 (2019).
33. F. Ding, Q. B. Mou, Y. Ma, G. F. Pan, Y. Y. Guo, G. S. Tong, C. H. J. Choi, X. Y. Zhu, C. Zhang, A crosslinked nucleic acid nanogel for effective siRNA delivery and antitumor therapy. *Angew. Chem. Int. Edit.* **57**, 3064–3068 (2018).
34. J. Li, H. Pei, B. Zhu, L. Liang, M. Wei, Y. He, N. Chen, D. Li, Q. Huang, C. H. Fan, Self-assembled multivalent DNA nanostructures for noninvasive intracellular delivery of immunostimulatory CpG oligonucleotides. *ACS Nano* **5**, 8783–8789 (2011).
35. W. Wu, D. Mao, F. Hu, S. Xu, C. Chen, C.-J. Zhang, X. Cheng, Y. Yuan, D. Ding, D. Kong, B. Liu, A highly efficient and photostable photosensitizer with near-infrared aggregation-induced emission for image-guided photodynamic anticancer therapy. *Adv. Mater.* **29**, 1700548 (2017).
36. G. Diaz, S. Liu, R. Isola, A. Diana, A. M. Falchi, Mitochondrial localization of reactive oxygen species by dihydrofluorescein probes. *Histochem. Cell Biol.* **120**, 319–325 (2003).
37. X. Chen, Z. Zhong, Z. Xu, L. Chen, Y. Wang, 2′,7′-dichlorodihydrofluorescein as a fluorescent probe for reactive oxygen species measurement: Forty years of application and controversy. *Free Radic. Res.* **44**, 587–604 (2010).
38. W. Keller, R. Crouch, Degradation of DNA/RNA hybrids by ribonuclease H and DNA polymerases of cellular and viral origin. *Proc. Natl. Acad. Sci. U.S.A.* **69**, 3360–3364 (1972).
39. Y. Baglo, A. J. Sorrin, B. J. Liang, H. C. Huang, Harnessing the potential synergistic interplay between photosensitizer dark toxicity and chemotherapy. *Photochem. Photobiol.* **96**, 636–645 (2020).
40. D. B. Eckl, L. Dengler, M. Nemmert, A. Eichner, W. Bäumler, H. Huber, A closer look at dark toxicity of the photosensitizer TMPyP in bacteria. *Photochem. Photobiol.* **94**, 165–172 (2018).
41. C. Donohoe, M. O. Senge, L. G. Arnaut, L. C. Gomes-da-Silva, Cell death in photodynamic therapy: From oxidative stress to anti-tumor immunity. *Biochim. Biophys. Acta Rev. Cancer* **1872**, 188308 (2019).
42. J. Nam, S. Son, K. S. Park, W. P. Zou, L. D. Shea, J. J. Moon, Cancer nanomedicine for combination cancer immunotherapy. *Nat. Rev. Mater.* **4**, 398–414 (2019).

43. A. P. Castano, P. Mroz, M. X. Wu, M. R. Hamblin, Photodynamic therapy plus low-dose cyclophosphamide generates antitumor immunity in a mouse model. *Proc. Natl. Acad. Sci. U.S.A.* **105**, 5495–5500 (2008).
44. C. Sun, R. Mezzadra, T. N. Schumacher, Regulation and function of the PD-L1 checkpoint. *Immunity* **48**, 434–452 (2018).
45. M. J. O'Shaughnessy, K. S. Murray, S. P. La Rosa, S. Budhu, T. Merghoub, A. Somma, S. Monette, K. Kim, R. B. Corradi, A. Scherz, J. A. Coleman, Systemic antitumor immunity by PD-1/PD-L1 inhibition is potentiated by vascular-targeted photodynamic therapy of primary tumors. *Clin. Cancer Res.* **24**, 592–599 (2018).
46. R. Bao, Y. Wang, J. Lai, H. Zhu, Y. Zhao, S. Li, N. Li, J. Huang, Z. Yang, F. Wang, Z. Liu, Enhancing anti-PD-1/PD-L1 immune checkpoint inhibitory cancer therapy by CD276-targeted photodynamic ablation of tumor cells and tumor vasculature. *Mol. Pharm.* **16**, 339–348 (2019).
47. R. Zhang, Z. Zhu, H. Lv, F. Li, S. Sun, J. Li, C. S. Lee, Immune checkpoint blockade mediated by a small-molecule nanoinhibitor targeting the PD-1/PD-L1 pathway synergizes with photodynamic therapy to elicit antitumor immunity and antimetastatic effects on breast cancer. *Small* **15**, e1903881 (2019).
48. M. Barry, R. C. Bleackley, Cytotoxic T lymphocytes: All roads lead to death. *Nat. Rev. Immunol.* **2**, 401–409 (2002).
49. L. L. Feng, F. He, Y. L. Dai, B. Liu, G. X. Yang, S. L. Gai, N. Niu, R. C. Lv, C. X. Li, P. P. Yang, A versatile near infrared light triggered dual-photosensitizer for synchronous bioimaging and photodynamic therapy. *ACS Appl. Mater. Interfaces* **9**, 12993–13008 (2017).
50. C. H. Tung, M. S. Han, Y. Kim, J. J. Qi, B. E. O'Neill, Tumor ablation using low-intensity ultrasound and sound excitable drug. *J. Control. Release* **258**, 67–72 (2017).

Acknowledgments: We thank H. Li for AFM imaging and L. Di for CLSM imaging at the Instrumental Analysis Center of Shanghai Jiao Tong University. **Funding:** This work was financially supported by the National Key Research and Development Program of China (2018YFC1106102 and 2018YFA0902600), the National Natural Science Foundation of China (51973112, 51690151, 52103265, and 81871329), and the Science Foundation of the Shanghai Municipal Science and Technology Commission (18JC1410800 and 19JC1410300). **Author contributions:** C.Z. and Y.L. supervised the subject. Y.G. and C.Z. designed the study and experiments. Y.G. performed the experiments. X.Z. provided the apparatuses used in cell assay. Q. Zhu contributed to the analysis of the NMR data of PPA. Q. Zha., Q. Zhu, and J.G. contributed to the bioassays and in vivo antitumor immune evaluation. Y.G. and C.Z. wrote the draft manuscript. C.Z., H.Y., and Y.L. discussed the results and edited the manuscript. **Competing interests:** The authors declare that they have no competing interests. **Data and materials availability:** All data needed to evaluate the conclusions in the paper are present in the paper and/or the Supplementary Materials.

Submitted 17 November 2021
Accepted 3 March 2022
Published 20 April 2022
10.1126/sciadv.abn2941